Article:
Su, H, Bomans, PHH, Friedrich, H et al. (2 more authors) (2021) Crystallization via oriented attachment of nanoclusters with short range order in solution. Journal of Physical Chemistry C. ISSN 1932-7447

https://doi.org/10.1021/acs.jpcc.0c10323

Crystallization *via* Oriented Attachment of Nanoclusters with Short Range Order in Solution

Hao Su,[1,2] Paul H.H. Bomans,[1,2] Heiner Friedrich,[1,2,3] Yifei Xu[1,2,4] and Nico Sommerdijk[5]*

1. Laboratory of Materials and Interface Chemistry and Centre for Multiscale Electron Microscopy, Department of Chemical Engineering and Chemistry, Eindhoven University of Technology, PO box 513, 5600 MB, Eindhoven, The Netherlands
2. Institute for Complex Molecular Systems, Eindhoven University of Technology, PO Box 513, 5600 MB, Eindhoven, The Netherlands
3. Laboratory of Physical Chemistry and Centre for Multiscale Electron Microscopy, Department of Chemical Engineering and Chemistry, Eindhoven University of Technology, PO Box 513, 5600 MB, Eindhoven, The Netherlands
4. School of Chemistry, University of Leeds, Woodhouse Lane, LS2 9JT, Leeds, UK
5. Department of Biochemistry, Radboud Institute of Molecular Life Sciences, Radboud University Medical Center, Geert Grooteplein 6525 GA Nijmegen, The Netherlands

Corresponding Author

Dr. Yifei Xu

Email: Y.Xu4@leeds.ac.uk

Keywords: cryoTEM • non-classical crystallization • amorphous precursor • nanoclusters • cobalt complex

Abstract

Many mineral crystallization processes in aqueous solutions involve formation of nanoclusters with short range order. Their transformation into crystalline products is not well understood. Here we investigate the formation of long-range crystalline order within networks of cobalt-based nanoclusters. High-resolution cryogenic transmission electron microscopy (cryoTEM) together with NMR and FTIR spectroscopy shows the formation of ~0.8 nm sized $(Co)(NH_3)_5CO_3$ complexes at the initial stage. By ligand exchange, those complexes become bridged by CO_3^{2-}/OH^- ligands and form ~2 nm sized clusters, which subsequently aggregate into sheet-like networks due to the structural heterogeneity of the clusters. By further ligand change and adjustment in cluster orientations, long-range order is established, which leads to the nucleation of ammonium cobalt kambaldaite nanocrystals. Our observations demonstrate that nanoclusters with short range order can from crystals *via* an oriented-attachment pathway, which provides new insights into multi-step crystallization processes.

Introduction

Many mineral crystallization processes in solution involve the formation of metastable intermediates consisting of 1~2 nm sized clusters.[1-7] These clusters have been observed in a range of systems including calcium carbonate,[2-3] calcium phosphate,[4] calcium hydroxide,[5] calcium sulphate[6], zinc oxide[8] and iron oxide,[7] and they are usually considered to be 'amorphous' as they only display very broad signals in X-ray or electron diffraction analyses. However, the broadening of diffraction signals can also be attributed to the extremely small sizes of the clusters,[9] and the internal structures of the clusters are not necessarily disordered. In fact, short range order similar to what is observed in their larger, crystallized counterparts is often detected in these clusters,[3-4, 10] and it is still under debate whether these clusters should be regarded as 'amorphous clusters' or 'extremely small crystals'.[5, 9] In aqueous solution, these clusters can spontaneously transform into larger crystals,[2, 4] with the underlying transformation mechanisms far from being understood. One possible pathway is that these clusters dissolve into ions and then recrystallize, which has been shown for amorphous phases such as amorphous calcium carbonate (ACC).[11-12] Alternatively, clusters with short range orders may directly attach onto larger crystals, similar to the 'oriented-attachment' pathway observed for crystalline building blocks.[1, 13-15] Up to now, however, direct imaging of this transformation process for the nanoclusters remains unavailable.

Here we investigate the crystallization process of nanoclusters with short range order, using the carbonation of cobalt/ammonium complexes as a model system. Different from the commonly studied $CaCO_3$ formation process, this reaction starts from cobalt complexes with a well-defined short range order, which allows us to gain insight into the chemistry of the underlying transformation processes using NMR and Fourier-transform infrared spectroscopy (FTIR). By performing high resolution cryoTEM imaging on graphene oxide (GOx) coated grids,[16] the transformation process was visualized with sub-nanometer detail.

Materials and Methods

Materials

Analytical grade $CoCO_3$, $(NH_4)_2CO_3$ and 32% ammonia solution were purchased from Sigma Aldrich and used without further purification. Ultrapure water for preparation of graphene oxide (GOx) TEM grids, and D_2O for NMR experiments were purchased from VWR. Deionized water (18.2 mΩ) obtained from a Millipore system was used for chemical reactions in this study.

Cryogenic Transmission Electron Microscopy

For conventional cryoTEM, 3 µL of the reaction solutions collected at different time points were applied to a lacey carbon cryoTEM grid and within 20 s plunge frozen using a vitrification robot (FEI Vitrobot™ Mark III, FEI Company) with 99 % humidity (Figure S1).[17] Prior to freezing, the cryoTEM grids were plasma treated using a Cressington Glow Discharge system for 45 s. Subsequently, the grid was plunged into liquid ethane which was maintained at approximately – 183 °C. The vitrified sample was then transferred to the TU/e cryoTITAN (FEI, FEG, 300 kV, Gatan Energy Filter, 2k x 2k Gatan CCD camera) and kept at liquid nitrogen temperatures at all times.

For the high-resolution cryoTEM imaging of the precursor phases, graphene oxide (GOx) support films were added to a Quantifoil R2/2 TEM grid (Figure S1) by: 1) diluting a 0.01 mg/mL GOx solution 2 times prior by vigorous stirring (purchased from Sigma Aldrich) and 2) applying the GOx solution to a hydrophilized TEM grids (glow discharged using a Cressington 208 carbon-coater for 40 seconds). By observing the grid at a low magnification at different regions we established that approximately 75% of the hole area was covered with GOx. For the vitrification of these grids, a mixture of 20% (v/v) isopropanol in ultrapure water was used in the humidifier of the Vitrobot. The grids were blotted for 5 seconds after a stabilization time of 5 seconds at 99% relative humidity. After blotting, another waiting time of 5 seconds at 99% relative humidity was applied. Subsequently, the grid was plunged into liquid ethane which was maintained at approximately –183 °C. Imaging on the GOx grids was done using a parallel beam with an illuminated area of 550 to 600

nm (nanoprobe TEM mode) at a dose of 60 $e^-/Å^2$ per image. The method significantly improves the image contrast of small objects with respect to conventional method (as shown in Figure S2). The nominal defocus for cryoTEM imaging was chosen by optimizing the contrast transfer function (CTF) to the object size as described in a previous study (see also Figure S3a).[16]

Nuclear Magnetic Resonance (NMR) Measurements

^1H liquid NMR spectra of reaction solutions were performed at the early stages of the reaction using a 500 MHz Varian Unity Inova NMR spectrometer. 60 mg $CoCO_3$ was dissolved in 2 mL of 32% ammonia solution. Subsequently 40 mg $(NH_4)_2CO_3$ was added into the solution and the mixture was diluted with D_2O to a total volume of 8.5 mL. The ammonia out-gassing reaction was allowed to proceed for 60 min. Subsequently, ~1 mL solution was taken at different time points and analyzed by NMR at room temperature. Spectrum analysis was done with MestReNova with the signal from H_2O and free NH_3 being subtracted first due to its high intensity.

UV-Vis spectroscopy and pH value measurement

UV-Vis spectra were acquired at room temperature on a Perkin-Elmer UV-Vis spectrometer Lambda 40 between 300 nm and 800 nm in 1 nm increments using a quartz glass cuvette with an optical path length of 1 mm. The samples were taken at different time points, cooled down and centrifuged at 20k rpm to remove the solids. The UV-Vis spectra were corrected using Milli-Q water as a background reference. The pH values of the reaction solutions were measured using a pH electrode connected to a Metrohm Tiamo system.

Fourier-Transform Infrared (FTIR) Spectroscopy Measurements of Freeze-Dried Samples

Attenuated total reflection (ATR) FTIR spectra of the crystallized and amorphous samples were measured directly on the freeze-dried powder sample using a Varian FTIR 3100 spectrometer with Golden Gate ATR accessory. To prepare the freeze-dried samples, reaction solutions were collected at 60 minutes and 24 hours, respectively. Solid products were separated from the reaction solution by centrifugation at 20k rpm, and then frozen in liquid nitrogen at -196 °C. The freeze-drying was then performed using a vacuum-assisted freeze-dryer (Labconco) with a cold trap for 24 hours. The temperature was set at -30 C and the pressure was at <0.22 mbar.

Powder X-ray Diffraction (pXRD)

pXRD measurements were carried out using a Rigaku Geigerflex powder diffractometer with Bragg-Brentano geometry using Cu radiation at 40 kV and 30 mA and a graphite monochromator to eliminate Cu K_β radiation. Solid products were separated from the reaction solution by centrifugation at 20k rpm and

subsequently freeze-dried to maintain their native state and then loaded on cover glasses. The pXRD patterns were acquired by step scans from 2θ = 5° to 2θ = 70° at a step size of 0.01°.

Size Measurements and Simulation of the Cobalt Complexes

The size of the cobalt complexes were determined by manually measuring in cryoTEM images with an in-house MATLAB script[4] both the long and short axis of approximately 80 individual complexes as seen in Figure S3b. The average of the short and long axis is considered as the diameter of the complex. Simulation of the complex structures were performed using Materials Studio (Accelrys Inc.) using VAMP package (a semi-empirical molecular orbital package for molecular organic and inorganic systems).[18] The calculations were performed using the PM6 Hamiltonian. The structure of the complex was built up based on the composition (e.g., 1 Co^{2+}, 5 NH_3 and 1 CO_3^{2-} for complex 1), and optimized using Jon Baker's Eigenvector Following (EF) routine (a built-in function in Material Studio). The solvent was set as H_2O. The accessible surface areas of the complexes and corresponding diameters (assuming that the complexes are spherical) were then calculated.

Results and Discussions

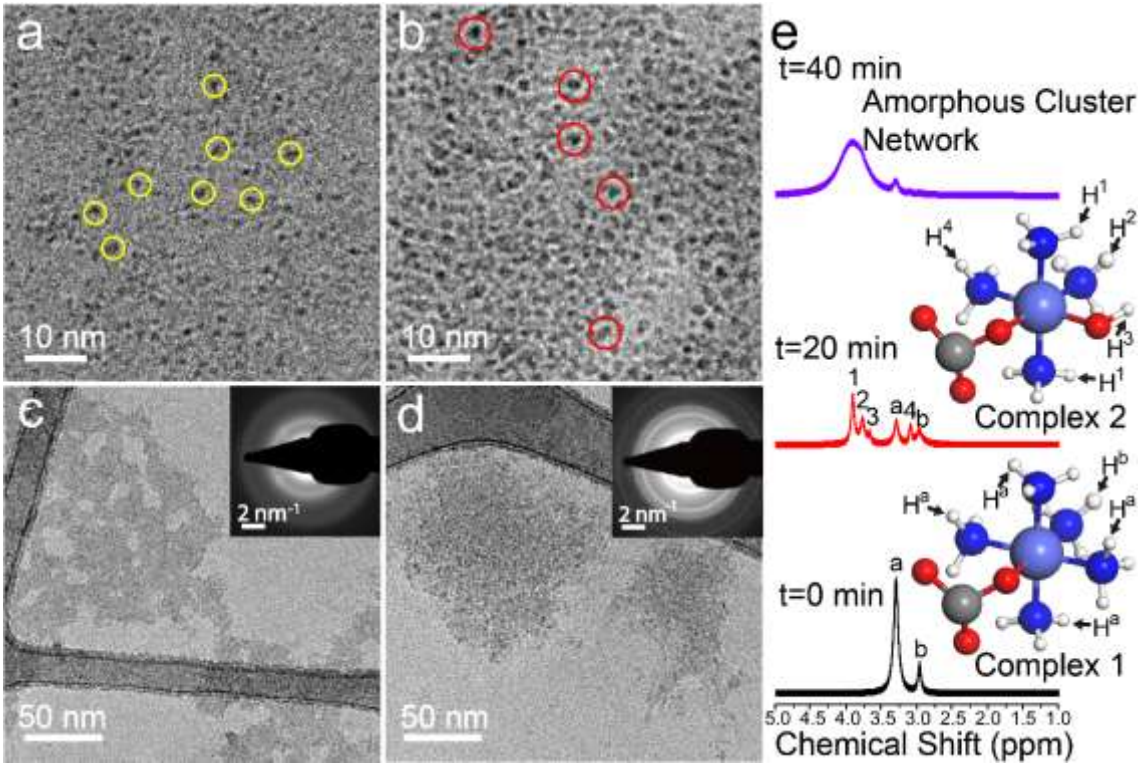

Figure 1. Morphological and structural development of the reaction products. (a-d) CryoTEM images at t= 0, 40, 60 and 80 min, respectively. Several ~0.8 nm complexes and ~2 nm clusters are highlighted by yellow and red circles in (a) and (b), respectively. Inset of (c) and (d) are corresponding LDSAED patterns. GOx grids were used for (a) and (b) and lacey carbon film grids were used for (c) and (d). (e) ^1H NMR spectra of the reaction solution at t=0, 20, and 40 min, respectively, and the simulated structures of complex 1, $Co(II)(NH_3)_5CO_3$, and complex 2, cis-$Co(II)(NH)_4CO_3OH$, respectively.

To perform the carbonation of Co(II)/NH_3 complexes, 1.8 g $CoCO_3$ was dissolved in 60 ml of 32% ammonia solution.[19] Subsequently, 12 g $(NH_4)_2CO_3$ was added and the mixture was diluted to 250 ml in a Teflon coated flask to prevent heterogeneous nucleation. The reaction solution was then heated at 90 °C for 24 hours. The color and pH value of the solution was monitored during the reaction (Figure S4), which shows that the solution changed from brown (pH ~ 9.8), to dark red (1 hour, pH 8.5) to violet (2 hours, pH 8.4) and eventually before became colorless (24 hours, pH 7.8) with black precipitates formed at the bottom. UV-Vis analysis of the reaction solutions (Figure S5a) indicated absorption bands at 375 nm and 525 nm, which is attributed to the d orbital splitting of Co due to the formation of Co(II)/NH_3 complex.[20] The intensities of two absorption peaks are proportional to the Co(II) concentration, and therefore can be used to monitor the change of Co(II) concentration following a calibration curve (Figure S5b).[21] It can be seen that overall the cobalt (II) concentration decreased during the first 120 min with a small increase observed at 80 min (Figure S4).

The early-stage products (t≤ 40 min) were imaged on GOx coated TEM grids, improving resolution and contrast in cryoTEM (Figures S1 and S2).[16] Objects with diameters of only 8.4 ± 1.2 Å were observed immediately (actual t=15~20 s, see Materials and Methods for details) after preparation of the reaction solution (Figure 1a, Figure S3b). Liquid phase ^{1}H NMR indicated two peaks, H^a at 3.31 ppm and H^b at 2.96 ppm respectively, with a peak area ratio of 4:1. The ^{1}H chemical shifts of species in metal complex are strongly affected by the solution environment, and it is therefore difficult to directly assign the peaks based on chemical shift values. However, it has been reported for Co/NH_3 complexes that when a NH_3 ligand is replaced by another ligand, the ^{1}H NMR signal from the protons at the cis- positions will shift to the lower field, while the trans-proton signal will shift to the higher field.[22-23] Taking this effect into account, and considering the chemistry of the reaction solution and the ratio between the two peaks, the signals suggest the formation of Co(II)$(NH_3)_5CO_3$ complexes (complex1 in Figure 1e), which has 4 NH_3 (12 protons) at the cis- positions and 1 NH_3 (3 protons) at the trans- position with respect to the CO_3^{2-}. To further confirm this, we simulated the structure of the complex 1(see Materials and Methods for details),[18] which determined the accessible surface area of the complex to be 230 Å^2, corresponding to a diameter of 8.5 Å, and matching well with the cryo-TEM observations. After 20 mins, 4 new peaks appeared in the ^{1}H NMR spectra (H^{1-4}, Figure 1e) at 3.93, 3.79, 3.68 and 3.10 ppm, respectively, co-existing with the initial two peaks for H_a and H_b. The relative areas of the new peaks were H^1:H^2:H^3:H^4 ≈ 6:3:1:3. Considering the structure of complex 1 and the ratio between the peaks, the signals could only be assigned to cis-Co(II)$(NH)_4CO_3OH$ (complex 2 in Figure 1e), with a cis- NH_3 in complex 1 being replaced by OH^-, introducing 4 populations of protons in the structure with a ratio of 6:3:1:3 as indicated in Figure 1e. While the trans- /cis- effect of different ligands on ^{1}H NMR signal highly depends on the solution environment,[23] our results suggest that the effect of OH^- is stronger than CO_3^{2-} in our experiment. As a result, the signal of H^1 is shifted most to the lower field with respect to

H_a, as they are adjacent to both the OH^- and the CO_3^{2-}. Meanwhile, the signal of H^2 is also shifted to the left side of H^a due to the stronger cis- effect of OH^-. H^4, on the other hand, are at the trans- position of the OH^-, and their signal is therefore shifted to the right side of H^a due to the strong trans- effect of OH^-, resulting the chemical shift sequence of the peaks. CryoTEM showed no change for the average size of the new complexes at t=20 min, in agreement with simulations that predict a diameter of 8.3 Å for complex 2.

During the next 20 min of reaction, cryoTEM showed that the complexes developed into networks of loosely aggregated ~2 nm sized clusters (Figure 1b). Concomitantly, the H^{1-4} peaks in the ^1H NMR spectra became obscured by a broad signal (Figure 1e), while the intensity of $H^{a,b}$ peaks decreased significantly, indicating a rapid exchange of protons between the NH_3/OH species, most likely due to a closer distance between them within the network. Subsequently, the network became denser at t=60 min and formed discontinuous thin sheets (Figure 1c). The composition of this sheet could no longer be analyzed by liquid NMR due to further peak broadening. Despite its sheet-like morphology, this phase did not show any sign of crystallinity in low-dose selected area electron diffraction (LDSAED, inset of Figure 1c), i.e, it is diffractionally amorphous. This was further confirmed by powder X-Ray diffraction (PXRD) on a freeze-dried sample (Figure 2a top).

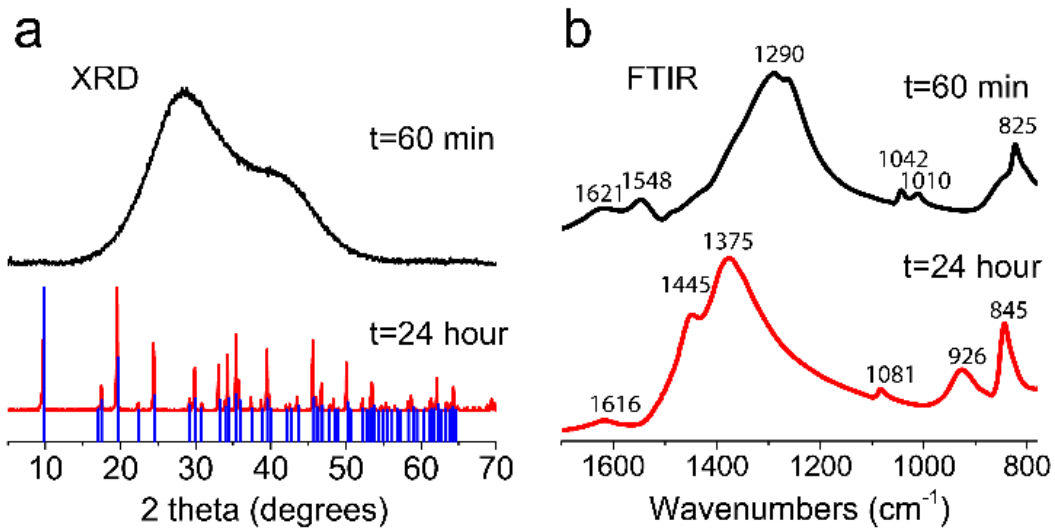

Figure 2. (a) Powder XRD of the freeze-dried sample at 60 min (top) and 24 hours (bottom). (b) FTIR of the freeze-dried sample at 60 min (top) and 24 hours (bottom).

After 80 min eventually a polycrystalline LDSAED pattern was obtained (inset Figure 1d), which matched the diffraction pattern reported for ammonium cobalt kambaldaite (ACK, or $(NH_4)_2Co(II)_8(CO_3)_6(OH)_6{\cdot}4H_2O$).[24] The final solid product was collected after 24 hours (Figure S6), and the PXRD pattern of the product confirmed the formation of polycrystalline ACK (Figure 2a bottom). The chemical compositions of freeze-dried samples were investigated by FTIR (Figure 2b) after 60 min and 24 hours of reaction, respectively. The 60 min sample showed a broadband at ~1300 cm^{-1} attributed to an

overlapping of the NH_3 δ_s mode and CO_3^{2-} ν_1 mode vibrations.[25] The signal at 1548 cm^{-1} could be assigned to the NH_3 δ_a mode, while the signals at 1042 and 825 cm^{-1} were assigned to the ν_2 and ν_6 modes of CO_3^{2-}, respectively. The minor signals at 1621 cm^{-1} and 1010 cm^{-1} were attributed to the bending modes of surface water and Co-OH, respectively.[26] These results confirm that the sample indeed contained NH_3, CO_3^{2-} and OH^- ligands, with a bonding typical for cobalt complexes. For the 24-hour sample (Figure 2b bottom), however, the strongest signals were the vibrations at 1445 and 1375 cm^{-1}, corresponding to the splitting of CO_3^{2-} ν_3 mode, indicating that the symmetry of CO_3^{2-} has decreased due to crystallization.[26] This also explains the absence of CO_3^{2-} ν_1 mode, and the shift of (Co-OH) signal to 926 cm^{-1}. At the same time, the NH_3 δ_a and δ_s signals were no longer visible, indicating that there were no Co-NH_3 bonds in the crystallized sample,[25] in line with the crystal structure of ACK (Figure 4a).[24]

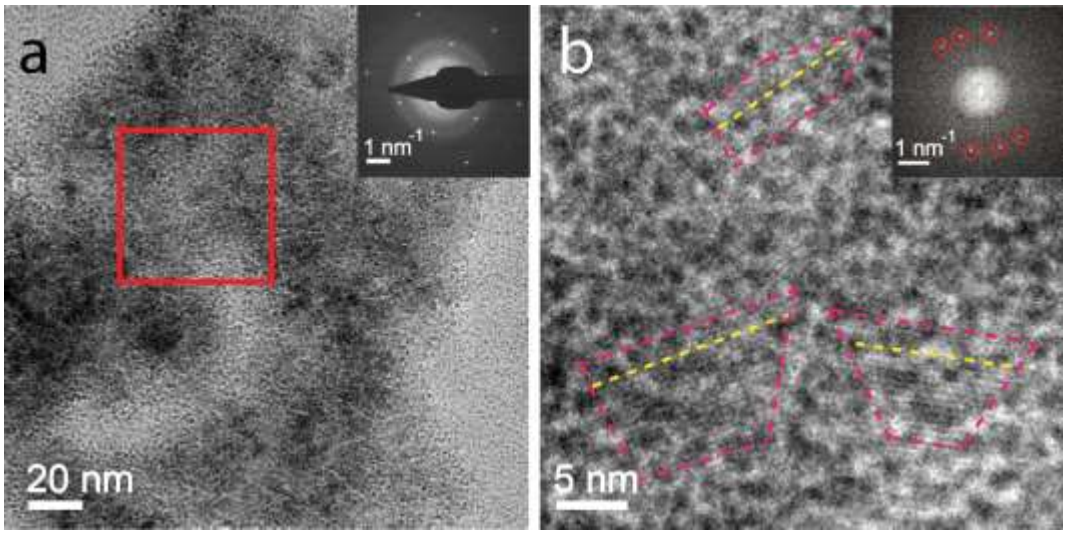

Figure 3. High-resolution cryoTEM images of the 60 min product on GOx grids. (a) Denser sheet surrounded by 2 nm clusters are seen. The inset shows the LDSAED pattern recorded after high-resolution imaging with only diffraction spots of single layer GOx being present. (b) Enlargement of the area in the red square in (a). Three regions showing lattice fringes are enclosed by magenta dashed lines. The orientations of the lattice fringes are indicated by yellow dashed lines. In the inset, the FFT of the image shows 3 pairs of spots corresponding to the lattice fringes in the 3 regions, respectively.

The 60 min product was further examined by high-resolution cryoTEM on GOx grids to determine how crystals developed within the network of nanoclusters. Denser sheets composed of, and surrounded by, 2 nm clusters were observed (Figure 3a). LDSAED patterns of the sheets (inset of Figure 3a) recorded after high-resolution imaging only showed broad rings (in addition to the GOx diffraction pattern), indicating that most of the product was still diffractionally amorphous even after electron beam exposure. However, within the sheets, ~10 nm sized regions embedded within the network of the clusters displaying lattice fringes were detected (Figure 3b). Fast Fourier transformation (FFT) shows 3 pairs of spots corresponding to the lattice fringes in the 3 regions in the image, respectively (Figure 3b, inset). The spots are in different orientations

but have a uniform d-spacing of 5.04 ± 0.1 Å, matching the (011) plane of ACK and revealing that these regions are randomly oriented ACK nanocrystalline domains. Notably, image intensity of these regions are not different from the areas with no lattice fringe, indicating that the ACK nanocrystalline domains are not thicker or denser. Therefore, these crystals unlikely nucleated on top of the surface of the nanocluster network, but did develop within it, most probably by rotating and bridging the clusters.

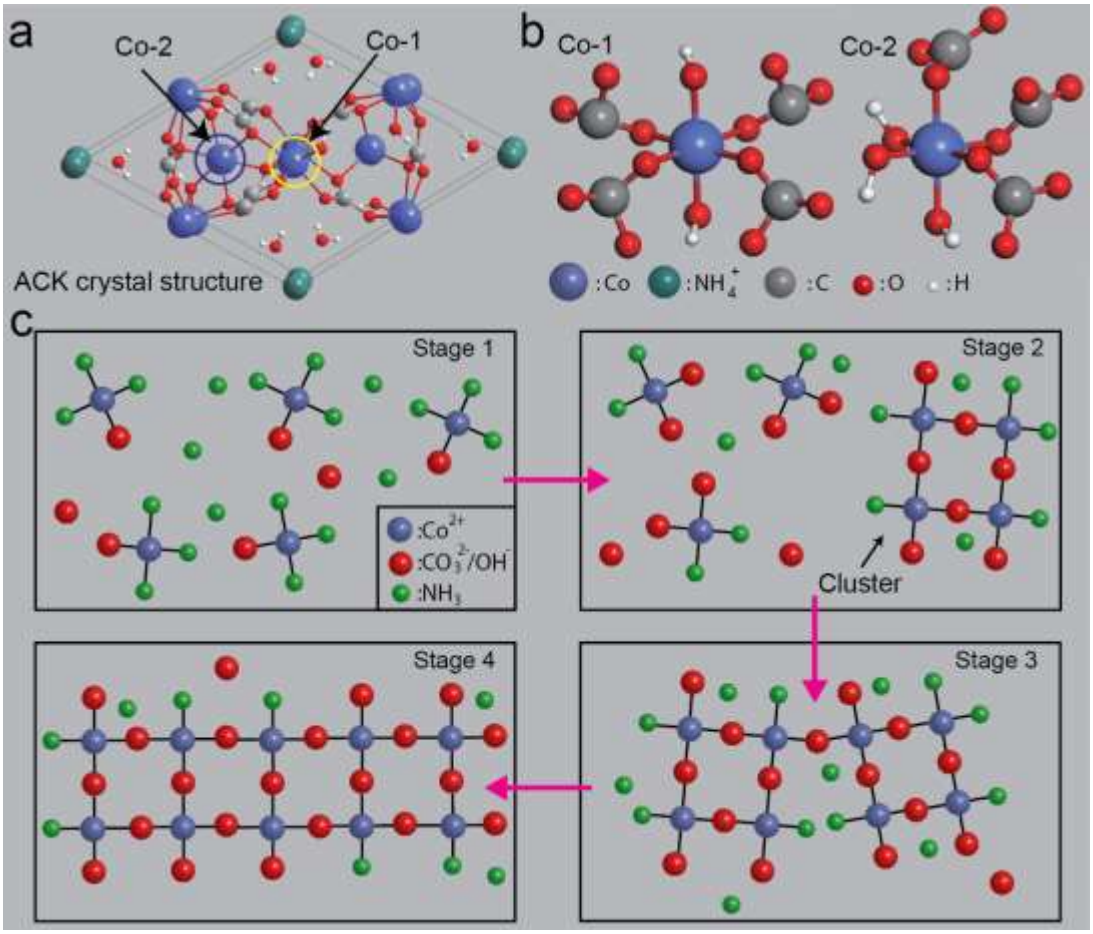

Figure 4. (a) Schematics of atomic positions in ACK crystal structure. Two types of Co atoms, Co-1 and CO-2, are highlighted by blue and yellow circles, respectively. (b) Specific coordination environment for Co-1 and Co-2 atomic positions. (c) 2D Schematics of the transformation process starting from complexes *via* clusters to crystals.

To further understand the crystallization process, the ACK crystal structure was examined (Figure 4a).[24] ACK contains two types of Co atoms (Co-1 and Co-2), which are both 6-coordinated with CO_3^{2-} or OH^-, forming an octahedral geometry (Figure 4b). These octahedrons are bridged by CO_3^{2-} and OH^-, while NH_4^+ only resides in the structure to balance the charges. Similarly, all of the Co(II) complexes observed during the reaction were also 6-coordinated, with the anisotropic $Co(II)(NH_3)_5CO_3$ complex as the starting point. While it is challenging to resolve the detailed structure and orientation of the ~2 nm clusters as they are diffractionally amorphous, we assume that the clusters also contain 6-coordinated Co atoms and have a short

range order similar to the ACK crystal. This would allow the clusters to crystallize by rotating and bridging rather than fully dissolving, as shown by our cryoTEM observations. Therefore, a crystallization process involving complexes and clusters rather than ions as building blocks seems to occur (Figure 4c). The NH_3 ligands, that are introduced to the central Co(II) ion in the initial ammonia-rich reaction environment, act as temporary "stabilizers" providing steric hindrance and facilitate the dissolution of the initial $CoCO_3$ salt (Stage 1). These NH_3 ligands are replaced during the reaction by OH^-/CO_3^{2-}, which act as "connectors" linking the Co (II) ions into ~2 nm sized clusters (stage 2). These clusters are expected to have a structure similar to ACK crystal, but are still covered by NH_3 ligands on their surfaces (as also suggested by the FTIR results in Figure 2b). Given the asymmetry of the complex, the subsequent ligand exchanges occur in positions adjacent to the initial CO_3^{2-}, according to the cis-effect commonly observed for 6-coordinated metal complexes.[23] This introduces directionality to the bridging process of the clusters, leading to the observed shape anisotropy of the sheet-shaped cluster networks (stage 3). Forced by their coordination geometry, clusters must rotate into optimized orientations to allow further bridges to be formed (Stage 3). Eventually, long-range order (nanocrystals) emerges when many clusters are rotated into orientations that match the crystal structure (Stage 4), i.e., when the clusters are orientedly attached together.

We propose this crystallization pathway may also apply for other clusters with short range orders similar to the latterly forming crystals, such as calcium carbonate clusters with calcite-like order,[3] or calcium phosphate clusters with atomic arrangement similar to octacalcium phosphate.[4, 27] A similar pathway was also proposed for the crystallization of calcium sulphate nanoclusters based on X-ray scattering results.[6] 'Stabilizer' for these clusters could be structural water or electrolytes in solution, while 'connectors' are the reacting ions on the cluster surface (e.g., carbonate, phosphate or sulphate). As it preserves pre-organized structures, this pathway should be kinetically more favorable than dissolution-recrystallization. However, we would like to emphasize the pathway is limited by several factors. First of all, the transformation rate of this pathway is obviously limited by the rotation dynamics of the clusters, which is significantly slower that ions in solution as shown by the liquid NMR results.[2] Besides, this pathway requires a continuous ligand exchange with the solution, which can only happen at the solid/liquid interface, and therefore will be hindered when the clusters are heavily bridged together. Another limiting factor is the number of available configurations of the clusters, and their match with the requirements of the final crystalline product; for example only complexes and clusters with the Co-1 or Co-2 structure match the ACK crystal structure. Non-matching complexes/clusters will have to first dissolve into ions before integration into the crystal is possible. Indeed, following a continuous decrease of the Co(II) concentration during the reaction, UV-Vis spectra (Figures S4 and S5) showed a temporary [Co(II)] increase at the onset of crystallization (at 80 min) before it decreased again until

the end of the reaction. This suggests that dissolution-recrystallization pathway still plays an important role, and explains why the final product is no longer sheet-like (Figure S6). This is similar to the transformation of calcium phosphate prenucleation complexes, which takes up Ca^{2+} from solution during mineralization.[4] Detailed titration experiments are required to determine the weight of this pathway in crystallization processes.

Conclusions

Our findings demonstrate that in solution, clusters with short range order can transform into crystalline materials *via* an oriented-attachment process, and shows that a dissolution-reprecipitation process must act in concert to complete the crystallization process. The results bring new insights into multi-step crystallization processes.

Supporting Information

Scheme comparing conventional and high-resolution cryo-TEM sample preparation methods; CryoTEM image of the 0 min sample prepared by the conventional method; Contrast transfer function (CTF) of cryoTitan at different defocus values; Particle size distribution of the 0 min sample; The color change of the reaction solution and concentration of the cobalt (II) ions obtained from UV-Vis absorption spectra; UV-Vis absorption spectra at different time points and calibration curve for analysis of cobalt (II) concentration; Scanning electron microscopy (SEM) image of the 24-hour sample.

Acknowledgments

The authors gratefully acknowledge Shell Global Solutions and the Netherlands Association of Scientific Research (NWO) for funding through the CHIPP program. The research of YX was supported by a Leverhulme research project grant (RPG-2017-178), and the Marie Curie Individual Fellowship (H2020-MSCA-IF-2019-885795-PolyTEM). The authors would like to thank Dr. Joseph Patterson (UC Irvine, USA) for helpful discussions on the GOx cryoTEM experiments.

Conflict of Interest

The authors declare no conflict of interest.

References

1. De Yoreo, J. J.; Gilbert, P. U. P. A.; Sommerdijk, N. A. J. M.; Penn, R. L.; Whitelam, S.; Joester, D.; Zhang, H.; Rimer, J. D.; Navrotsky, A.; Banfield, J. F. et al., Crystallization by Particle Attachment in Synthetic, Biogenic, and Geologic Environments. *Science* **2015**, *349*, aaa6760.

2. Xu, Y.; Tijssen, K. C.; Bomans, P. H.; Akiva, A.; Friedrich, H.; Kentgens, A. P.; Sommerdijk, N. A., Microscopic Structure of the Polymer-Induced Liquid Precursor for Calcium Carbonate. *Nat. Commun.* **2018**, *9*, 2582.
3. Sun, S.; Chevrier, D. M.; Zhang, P.; Gebauer, D.; Cölfen, H., Distinct Short-Range Order Is Inherent to Small Amorphous Calcium Carbonate Clusters (< 2 nm). *Angew. Chem. Int. Ed.* **2016**, *55*, 12206-12209.
4. Habraken, W. J. E. M.; Tao, J.; Brylka, L. J.; Friedrich, H.; Bertinetti, L.; Schenk, A. S.; Verch, A.; Dmitrovic, V.; Bomans, P. H. H.; Frederik, P. M. et al., Ion-Association Complexes Unite Classical and Non-Classical Theories for the Biomimetic Nucleation of Calcium Phosphate. *Nat. Commun.* **2013**, *4*, 1507-1507.
5. Rodriguez-Navarro, C.; Burgos-Cara, A.; Lorenzo, F. D.; Ruiz-Agudo, E.; Elert, K., Nonclassical Crystallization of Calcium Hydroxide Via Amorphous Precursors and the Role of Additives. *Cryst. Growth Des.* **2020**, *20*, 4418-4432.
6. Stawski, T. M.; Van Driessche, A. E.; Ossorio, M.; Rodriguez-Blanco, J. D.; Besselink, R.; Benning, L. G., Formation of Calcium Sulfate through the Aggregation of Sub-3 Nanometre Primary Species. *Nat. Commun.* **2016**, *7*, 1-9.
7. Baumgartner, J.; Dey, A.; Bomans, P. H.; Le Coadou, C.; Fratzl, P.; Sommerdijk, N. A.; Faivre, D., Nucleation and Growth of Magnetite from Solution. *Nat. Mater.* **2013**, *12*, 310.
8. van Rijt, M. M.; Oosterlaken, B. M.; Joosten, R. R.; Wijkhuijs, L. E.; Bomans, P. H.; Friedrich, H., Counter-Ion Influence on the Mechanism of HMTA-Mediated ZnO Formation. *CrystEngComm* **2020**, *22*, 5854-5861.
9. Williams, D. B.; Carter, C. B., The Transmission Electron Microscope. In *Transmission Electron Microscopy*, Springer: 1996; pp 3-17.
10. Gebauer, D.; Gunawidjaja, P. N.; Ko, J. P.; Bacsik, Z.; Aziz, B.; Liu, L.; Hu, Y.; Bergström, L.; Tai, C. W.; Sham, T. K., Proto-Calcite and Proto-Vaterite in Amorphous Calcium Carbonates. *Angew. Chem. Int. Ed.* **2010**, *49*, 8889-8891.
11. Bots, P.; Benning, L. G.; Rodriguez-Blanco, J.-D.; Roncal-Herrero, T.; Shaw, S., Mechanistic Insights into the Crystallization of Amorphous Calcium Carbonate (ACC). *Cryst. Growth Des.* **2012**, *12*, 3806-3814.
12. Nielsen, M. H.; Aloni, S.; De Yoreo, J. J., In Situ Tem Imaging of $CaCO_3$ Nucleation Reveals Coexistence of Direct and Indirect Pathways. *Science* **2014**, *345*, 1158-1162.
13. Niederberger, M.; Cölfen, H., Oriented Attachment and Mesocrystals: Non-Classical Crystallization Mechanisms Based on Nanoparticle Assembly. *Phys. Chem. Chem. Phys.* **2006**, *8*, 3271-3287.
14. Li, D.; Nielsen, M. H.; Lee, J. R.; Frandsen, C.; Banfield, J. F.; De Yoreo, J. J., Direction-Specific Interactions Control Crystal Growth by Oriented Attachment. *Science* **2012**, *336*, 1014-1018.
15. Mirabello, G.; Ianiro, A.; Bomans, P. H. H.; Yoda, T.; Arakaki, A.; Friedrich, H.; de With, G.; Sommerdijk, N. A. J. M., Crystallization by Particle Attachment Is a Colloidal Assembly Process. *Nat. Mater.* **2020**, *19*, 391-396.
16. van de Put, M. W. P.; Patterson, J. P.; Bomans, P. H. H.; Wilson, N. R.; Friedrich, H.; van Benthem, R. A. T. M.; de With, G.; O'Reilly, R. K.; Sommerdijk, N. A. J. M., Graphene Oxide Single Sheets as Substrates for High Resolution CryoTEM. *Soft Matter* **2015**, *11*, 1265-1270.
17. Patterson, J. P.; Xu, Y.; Moradi, M.-A.; Sommerdijk, N. A. J. M.; Friedrich, H., CryoTEM as an Advanced Analytical Tool for Materials Chemists. *Acc. Chem. Res.* **2017**, *50*, 1495-1501.
18. Beck, B.; Grummt, U.-W., Semiempirical Calculations of First-Order Hyperpolarizabilities: Testing the Performance of Different Methods in Comparison to Experiment. *J. Phys. Chem. B* **1998**, *102*, 664-670.
19. Bezemer, G. L.; Radstake, P. B.; Koot, V.; Van Dillen, A. J.; Geus, J. W.; De Jong, K. P., Preparation of Fischer-Tropsch Cobalt Catalysts Supported on Carbon Nanofibers and Silica Using Homogeneous Deposition-Precipitation. *J. Catal.* **2006**, *237*, 291-302.

20. Smith, D. W., Ligand Field Theory & Spectra. In *Encyclopedia of Inorganic Chemistry,* John Wiley & Sons, Ltd.: 2006.
21. Perkampus, H.-H., *UV-Vis Spectroscopy and Its Applications*; Springer Science & Business Media, 2013.
22. Jolly, W. L.; Harris, A. D.; Briggs, T. S., Proton Magnetic Resonance Spectra of Cobalt Ammine Complexes in Sulfuric Acid. *Inorg. Chem.* **1965**, *4*, 1064-1066.
23. Pratt, J.; Thorp, R.; Spectr, C. N. R., Cis and Trans Effects in Cobalt (III). *Adv. Inorg. Chem. Radiochem.* **1970**, 375.
24. Petrov, K., Preparation and Crystal Structure of the Ammonium Cobalt Carbonate Hydroxide Hydrate $(NH_4)_2Co_8(CO_3)_6(OH)_6 \cdot 4H_2O$. *Sol. Stat. Ion.* **1996**, *92*, 303-308.
25. Nakamoto, K., Infrared and Raman Spectra of Inorganic and Coordination Compounds, Sixth Edition. In *Handbook of Vibrational Spectroscopy*, John Wiley & Sons, Inc.: Hoboken, New Jersey, 2009.
26. Xu, R.; Zeng, H. C., Dimensional Control of Cobalt-Hydroxide-Carbonate Nanorods and Their Thermal Conversion to One-Dimensional Arrays of Co_3O_4 Nanoparticles. *J. Phys. Chem. B* **2003**, *107*, 12643-12649.
27. Fernandez-Martinez, A.; Lopez-Martinez, H.; Wang, D., Structural Characteristics and the Occurrence of Polyamorphism in Amorphous Calcium Carbonate. In *New Perspectives on Mineral Nucleation and Growth*, Springer: 2017; pp 77-92.

TOC Graphic